

Quantum criticality in a layered iridate

Kousik Samanta ¹, Jean C. Souza ¹, Danilo Rigitano¹, Adimir I. Morales ¹, Pascoal G. Pagliuso¹ & Eduardo Granado ¹✉

Iridates provide a fertile ground to investigate correlated electrons in the presence of strong spin-orbit coupling. Bringing these systems to the proximity of a metal-insulator quantum phase transition is a challenge that must be met to access quantum critical fluctuations with charge and spin-orbital degrees of freedom. Here, electrical transport and Raman scattering measurements provide evidence that a metal-insulator quantum critical point is effectively reached in 5% Co-doped Sr_2IrO_4 with high structural quality. The *dc*-electrical conductivity shows a linear temperature dependence that is successfully captured by a model involving a Co acceptor level at the Fermi energy that becomes gradually populated at finite temperatures, creating thermally-activated holes in the $J_{\text{eff}} = 1/2$ lower Hubbard band. The so-formed quantum critical fluctuations are exceptionally heavy and the resulting electronic continuum couples with an optical phonon at all temperatures. The magnetic order and pseudospin-phonon coupling are preserved under the Co doping. This work brings quantum phase transitions, iridates and heavy-fermion physics to the same arena.

¹“Gleb Wataghin” Institute of Physics, University of Campinas — UNICAMP, Campinas, SP, Brazil. ✉email: egranado@ifi.unicamp.br

A rare combination of strong spin–orbit coupling and substantial electron correlations in $5d^5$ iridates leads to exotic quantum states and remarkable physical phenomena such as spin liquid phases¹, Kitaev physics^{2–4}, Fermi arcs in the electronic structure with a possible connection to high- T_c superconductivity^{5–10}, and control of the crystal structure and magnetic properties by an electric current^{11,12}. An intensively investigated iridate is Sr_2IrO_4 (SIO), crystallizing in a tetragonal structure with an ABCD stacking of layers with tilted IrO_6 octahedra, as shown in Fig. 1a, b^{13,14}. As for the electronic structure, the octahedral crystal field splits the Ir $5d$ level into t_{2g} and e_g levels. The strong spin–orbit coupling breaks the sixfold degeneracy of the t_{2g} levels, giving rise to lower $J_{\text{eff}} = 3/2$ and upper $J_{\text{eff}} = 1/2$ sublevels. Finally, the $J_{\text{eff}} = 1/2$ -derived band is broken into lower and upper Hubbard bands, rendering SIO insulating^{15–17}. The Ir pseudospins order in a noncollinear magnetic structure below $T_N \sim 240$ K (see Fig. 1b)^{16,18,19}. Injection of charge carriers through electron or hole doping tends to reduce T_N , although it seems possible to destroy the insulating state without necessarily destroying the magnetic order²⁰ and vice-versa²¹. The most obvious approach to access the possible quantum critical fluctuations (QCF)^{22,23} associated with a metal–insulator transition would be to force the closure of the bandgap

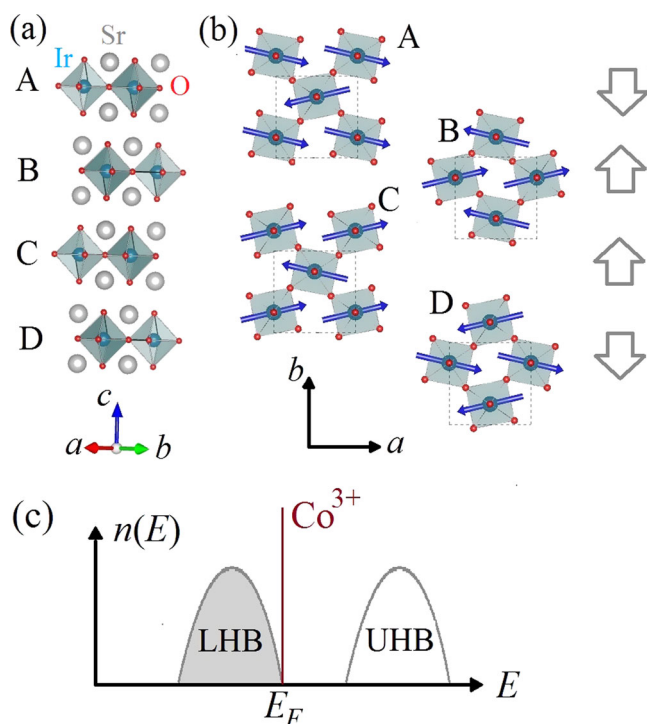


Fig. 1 Crystal, magnetic and electronic structures. **a** Crystal structure of Sr_2IrO_4 (SIO)^{13,14} (A–D layers are identified). **b** Detailed view of each layer projected into the ab plane, showing the rotation pattern of the IrO_6 octahedra and the orientation of the Ir magnetic moments^{16,18,19}. The net moment of each layer is indicated in the right, leading to the $\downarrow\uparrow\uparrow\downarrow$ stacking pattern at zero magnetic field. **c** Schematic density of states $n(E)$ of $\text{Sr}_2\text{Ir}_{0.95}\text{Co}_{0.05}\text{O}_4$ (SICO) near the Fermi level E_F , showing the $J_{\text{eff}} = 1/2$ lower and upper Hubbard bands (LHB and UHB) and a localized Co acceptor level. A metallic or Anderson insulating phase would arise if the energy $E_{\text{Co}^{3+}}$ of the acceptor level was located below E_F (corresponding to a Co^{3+} doping), whereas a gapped insulator would occur if instead this level was above E_F (corresponding to a Co^{4+} isoelectronic substitution). The quantum phase transition occurs where $E_{\text{Co}^{3+}} \sim E_F$, and the corresponding quantum critical fluctuations are electronic excitations from the lower Hubbard band to the acceptor level.

by application of external pressures. Nonetheless, the nonmetallic state persists up to at least 185 GPa despite the identification of exotic states at intermediate pressures^{24–29}. The alternative approach employed here involves the quest for a specific dilute cationic substitution that induces acceptor or donor impurity levels within the bandgap without actually charge doping the Ir-derived bands at $T = 0$ K, as shown in Fig. 1c. A possible contender might be the $\text{Sr}_2\text{Ir}_{1-x}\text{Rh}_x\text{O}_4$ system, as Rh and Ir are in the same group of the periodic table. However, it has been demonstrated that dilute Rh-substitution induces $\text{Rh}^{3+}/\text{Ir}^{5+}$ charge partitioning, in practice doping the system with holes and rapidly suppressing the magnetic order^{30–41}. Thus, the energy of the Rh^{3+} acceptor level is inferred to lay below the Fermi energy, $E_{\text{Rh}^{3+}} < E_F$, at least for $x < 0.24$. Another candidate is the $\text{Sr}_2\text{Ir}_{1-x}\text{Co}_x\text{O}_4$ system. Based on first principle calculations for $\text{Sr}_2\text{Ir}_{0.5}\text{Co}_{0.5}\text{O}_4$, it was inferred that $\text{Co}^{3+}/\text{Ir}^{5+}$ charge partitioning is energetically stable⁴², which was confirmed by subsequent experiments on this material^{43–45}. On the other hand, more dilute Co substitutions have not been investigated in much detail yet, although it is already known that even moderate Co substitution levels ($x \leq 0.1$) are not sufficient to reduce T_N appreciably⁴⁶. In this work, we investigate the charge transport, magnetic, structural, and vibrational properties of $\text{Sr}_2\text{Ir}_{0.95}\text{Co}_{0.05}\text{O}_4$ (SICO). We demonstrate that this material shows charge transport quantum critical behavior that is consistent with a simple picture where the Co^{3+} acceptor level coincides with the top of the lower Hubbard band at E_F (see Fig. 1c), triggering QCF with remarkably large renormalized masses.

Results

Structural characterization. X-ray powder diffraction profiles of SICO and SIO are shown for a selected angular interval in Fig. 2a, b, respectively. The whole profiles are shown in the Supplementary Figs. S1 and S2. Our data show asymmetric Bragg peak lineshapes in SICO (see Fig. 2b), revealing stacking faults⁴⁷. This is likely caused by the random contribution to the interatomic elastic potential caused by the Co substitution in SICO, disturbing the long-range ABCD stacking pattern of SIO (see Fig. 1a). The internal structural integrity of the layers is investigated by vibrational spectroscopy. Raman spectra of both samples are shown in Fig. 2c at $T = 20$ K. The main observed phonon modes, labeled as $M_1 - M_4$ ²⁶, show similar positions and lineshapes for both compounds, being only slightly broader for SICO. An additional feature is observed at ~ 340 cm^{-1} in SIO, indicative of a stoichiometric sample^{48,49}, whereas in SICO this feature is washed out and broad additional signals are observed at ~ 260 and ~ 420 cm^{-1} . The 260 cm^{-1} peak was previously observed and becomes stronger in more disordered samples^{48,49}. The weak intensity of the additional Raman features associated with disorder and the relatively sharp $M_1 - M_4$ modes in SICO indicate that the individual layer structures are preserved to a large extent through the 5% Co substitution, in contrast to the $\text{Sr}_2\text{Ir}_{1-x}\text{Ru}_x\text{O}_4$ series that shows much larger modifications in the phonon Raman spectra even at low doping levels⁴⁹.

Charge transport at zero magnetic field. The electrical resistivity curves $\rho(T)$ of SIO and SICO are shown in Fig. 3a. The values of $\rho(T)$ are significantly reduced for SICO with respect to the parent compound. In addition, the temperature dependence of the former is remarkably well captured by a simple power-law behavior, $\rho(T) = A^{-1} \cdot T^{-x}$ with $x = 1.075(1)$, over the entire investigated temperature interval $3 < T < 300$ K (dashed line in Fig. 3a). Such power-law behavior is not found in SIO (see Supplementary Fig. S3). Figure 3b displays the same data in terms of electrical conductivity $\sigma(T)$ in a double-log scale for SICO only. The fit to

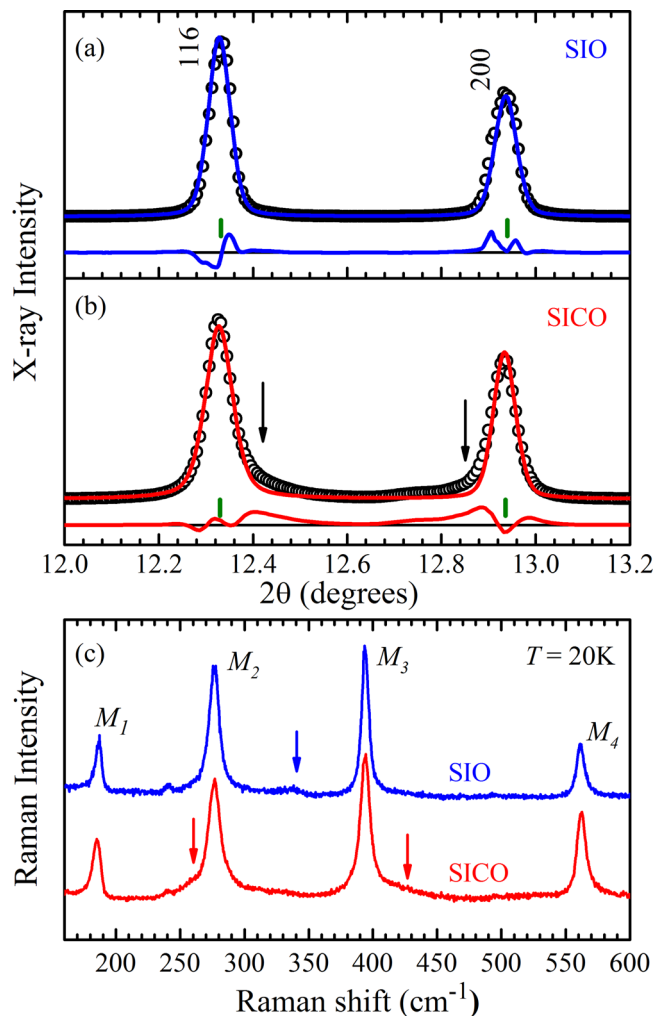


Fig. 2 Structural characterization. Selected portion of the X-ray diffraction profiles of Sr_2IrO_4 (SIO, **a**) and $\text{Sr}_2\text{Ir}_{0.95}\text{Co}_{0.05}\text{O}_4$ (SICO, **b**) at room temperature ($\lambda = 0.61986 \text{ \AA}$), covering the 116 and 200 Bragg reflections marked by the short vertical bars. The open symbols are experimental data and the solid lines are calculated profiles after a Rietveld refinement using pseudo-Voigt lineshapes for the individual Bragg peaks. The difference profiles are shown at the bottom of each figure. The vertical arrows in (**b**) highlight the asymmetric lineshape broadening. **c** Unpolarized Raman scattering spectra of the two investigated samples at $T = 20 \text{ K}$. The vertical arrows highlight the presence of a peak at $\sim 340 \text{ cm}^{-1}$ for SIO that is indicative of a stoichiometric sample^{48, 49}, and extra features at ~ 260 and $\sim 420 \text{ cm}^{-1}$ for SICO that are associated with weak disorder.

the low-temperature data ($T < 6 \text{ K}$) is optimized by a slightly different exponent $x = 1.003(6)$ that is even closer to unity. Note that the positive exponent implies that $\sigma \rightarrow 0$ as $T \rightarrow 0$, i.e., the material is nonmetallic. On the other hand, an exponential behavior $\sigma(T) \propto \exp[-(T_0/T)^\alpha]$ is expected for insulating materials, with $1/4 \leq \alpha \leq 1$ for either a bandgap insulator ($\alpha = 1$) or for a variable range hopping mechanism where the specific α is defined by the system dimensionality and the specific energy-dependence of the density of states $n(E)$ near E_F ⁵⁰. Neither of such exponential behaviors for $\sigma(T)$ are observed for SICO (see Supplementary Fig. S4), so this material is not classified either as a Mott, Slater or an Anderson insulator. Actually, according to very general scaling considerations, a power-law behavior $\sigma(T) \propto T^x$ signals a metal-insulator quantum phase transition²². The positive exponent contrasts with the negative values found in metallic materials where the quantum criticality is not due to the

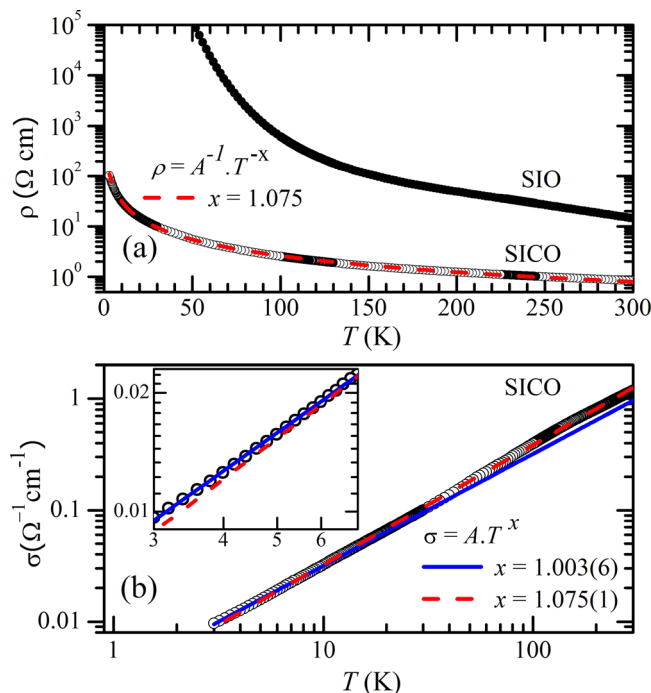


Fig. 3 Transport data at zero magnetic field. **a** Temperature dependence of the electrical resistivity $\rho(T)$ of Sr_2IrO_4 (SIO) and $\text{Sr}_2\text{Ir}_{0.95}\text{Co}_{0.05}\text{O}_4$ (SICO). The dashed line is the fitted power-law behavior $\rho(T) = A^{-1} \cdot T^{-x}$, where A and $x = 1.075(1)$ are fitting constants, revealing that SICO is at the onset of a metal-insulator quantum phase transition. **b** Electrical conductivity $\sigma(T)$ in a double-log scale. The inset is a zoom out at low temperatures. The dashed and solid lines correspond to fits to $\sigma(T) = A \cdot T^x$ with $x = 1.075(1)$ and $x = 1.003(6)$, respectively, where the latter exponent was obtained from fitting low-temperature data only ($T < 6 \text{ K}$). Errors in parentheses are statistical only and represent one standard deviation obtained from the corresponding fit.

proximity of a metal-insulator transition but interfaces two different conducting states, such as in a magnetic/heavy fermion quantum phase transition^{51,52}. The specific value $x \sim +1$ for SICO must be captured by an appropriate microscopic model (see below).

Magnetic properties and magnetoresistance. Magnetization $M(T)$ curves of SICO and SIO are shown in Fig. 4a, taken on warming after zero-field cooling and warming after field cooling, with $H = 5 \text{ kOe}$. Both compounds order at $T_N \sim 240 \text{ K}$, in line with ref. 46. The shapes of the $M(T)$ curves of SIO and SICO are distinct and the magnetization values are substantially reduced by the Co substitution. The latter result either indicates that the Co moments partially compensate the Ir net moments or the magnetic canting angle of the Ir moments (see Fig. 1b) is reduced for SICO. Also, both materials feature a separation of the zero-field cooling and warming after zero-field cooling curves that becomes more prominent below $T \sim 100 \text{ K}$ ⁵³. This is understood in terms of a field-induced transition of the $\downarrow\uparrow\downarrow$ magnetic structure and symmetry-related domains at zero-field to $\uparrow\uparrow\uparrow$ under an applied field along the ab -plane $H_{ab} \sim 2 \text{ kOe}$ ^{16,48,54}. In a polycrystal, the H_a projection is different for each crystallite, and with an external field $H = 5 \text{ kOe}$ a substantial fraction of the crystallites will still have $H_a < 2 \text{ kOe}$, leading to a coexistence of different phases at low temperatures in proportions that are arguably sensitive to the thermomagnetic sample history. This is manifested not only in the different zero-field cooling and warming after zero-field

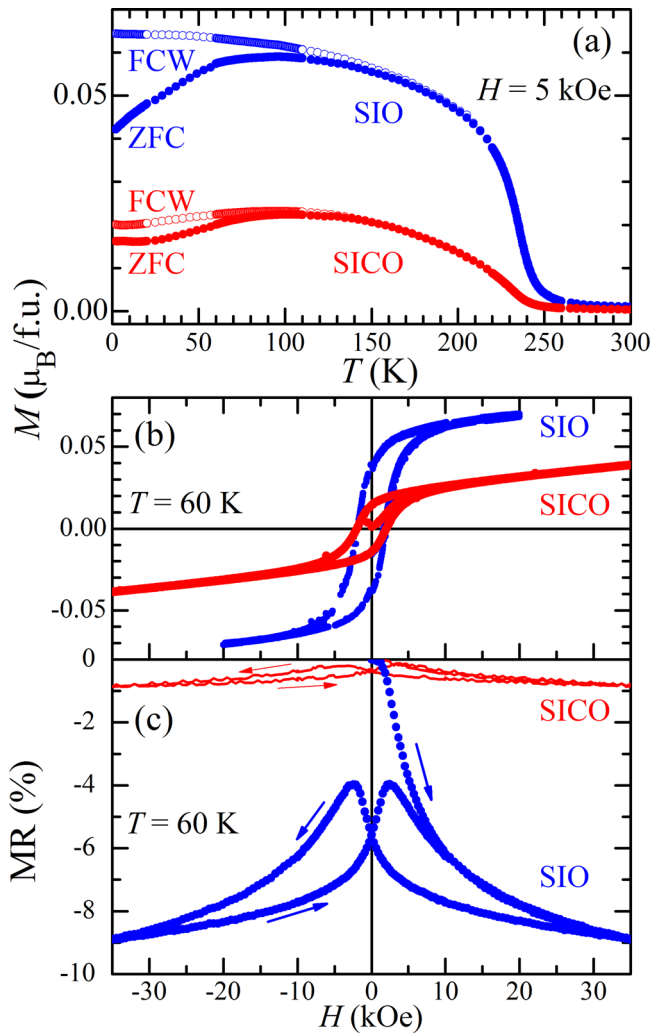


Fig. 4 Magnetization and magnetoresistance. **a** Temperature dependence of the magnetization $M(T)$ of Sr_2IrO_4 (SIO) and $\text{Sr}_2\text{Ir}_{0.95}\text{Co}_{0.05}\text{O}_4$ (SICO) taken on warming with a magnetic field $H = 5$ kOe that is applied after zero-field cooling (ZFC) or field cooling (FCW). **b** H -dependence of magnetization and magnetoresistance $\text{MR} \equiv [\rho(H) - \rho(H = 0)]/\rho(H = 0)$ (**c**) for both materials at $T = 60$ K, where $\rho(H)$ is the magnetic-field dependent electrical resistivity.

cooling $M(T)$ curves, but also in the hysteresis of the isothermal $M(H)$ curves (see Fig. 4b and ref. 13).

Figure 4c shows the magnetoresistance of SIO and SICO at $T = 60$ K taken after zero-field cooling (see Supplementary Fig. S5 for magnetoresistance at other temperatures). SIO shows a substantial negative magnetoresistance of $\sim 9\%$ for $H = 35$ kOe. A field-hysteretic behavior is also observed. This phenomenon is again originated in the field-induced transition between the $\downarrow\uparrow\downarrow$ and $\uparrow\uparrow\uparrow$ structures, where the former is substantially more resistive²⁰. Remarkably, the initial high-resistance state is not recovered by cycling the field. This is likely due to a powder distribution of internal fields that are created after the $\uparrow\uparrow\uparrow$ state is first activated, which may prevent the homogeneous high-resistance $\downarrow\uparrow\downarrow$ state to be simultaneously recovered over the entire sample volume. The magnetoresistance of SICO is largely suppressed with respect to SIO (see Fig. 4c), remaining below 1% up to $H = 35$ kOe. This indicates that, for SICO, the additional electronic scattering channel introduced by the Co impurities reduces the mean-free path of the thermally-activated charge carriers, overwhelming the magnetic scattering channel that is

responsible for the large magnetoresistance of SIO. We therefore estimate that the electronic mean free path of SICO is $D \sim 8 \text{ \AA}$, which is the average separation between the Co scattering centers for 5% substitution. We should note that in SIO the conductivity in the ab plane is higher than along c ^{20,55}. Thus, in polycrystals the resistivity and magnetoresistance curves are presumably dominated by the charge transport in the ab plane. This is also likely valid for SICO, although this assumption is not essential for the conclusions of this work.

Electron-phonon and pseudospin-phonon couplings. We now return to a more detailed investigation of the Raman spectra (Fig. 2c and Supplementary Fig. S6). The M_1 lineshape of SICO is fitted to the Fano expression $I(\omega) = I_0(q + \epsilon)^2/(1 + \epsilon^2)$, where I_0 is the intensity, $\epsilon = (\omega - \omega_0)/\Gamma$, ω_0 and Γ are the phonon frequency and linewidth, respectively, and $1/q$ is the asymmetry parameter that measures the coupling of the phonons with the electronic continuum⁵⁶ (see Fig. 5a). In opposition to SICO, the M_1 lineshape for SIO is symmetric at low temperatures, in agreement with previous studies^{57,58}. Figure 5b shows the temperature dependence of $|1/q|$ for mode M_1 of SICO. A substantial asymmetry parameter $|1/q| = 0.15$ is observed at the base temperature. This reveals a continuum of low-energy excitations at $T \rightarrow 0$ that is not present in SIO. Considering that a hypothetical metallic state in SICO is dismissed by resistivity data, this result indicates that the insulating gap in SICO must be below ~ 0.02 eV, placing this material very close to a quantum critical point. The $|1/q|$ parameter tends to increase on warming, with anomalies at $T \sim 100$ K and $\sim T_N$. In particular, the anomaly at $T \sim 100$ K suggests there is another physically meaningful temperature below T_N for SICO, as previously inferred for SIO^{12,20,53,59,60}. The reduced magnetization below ~ 100 K also supports this conclusion (see Fig. 4a).

Figure 5c shows the temperature dependence of the frequency of the M_3 mode for SIO and SICO fitted with Lorentzian lineshapes ($|1/q| = 0$), in comparison to the expected anharmonic behavior $\Delta\omega_{\text{anh}}(T) = A[1 + 2/(e^{\hbar\omega_0/2k_B T} - 1)]$ ⁶¹. Both compounds show anomalous shifts of this mode below T_N . This result is ascribed to the pseudospin-phonon coupling effect^{62–64}. The anomalous hardenings after subtraction of the anharmonic term are shown in Fig. 5d. The magnitude of the pseudospin-phonon anomaly is not reduced for SICO in comparison to SIO, indicating that the microscopic magnetic network of Ir pseudospins is still well preserved in SICO. The other $M_1 - M_4$ phonon parameters are shown in the Supplementary Fig. S7.

Discussion

We propose the schematic energy diagram displayed in Fig. 1c to explain our experimental results. The quantum critical point occurs as the localized Co^{3+} acceptor level matches the top of the lower Hubbard band at E_F . At low temperatures, the Co^{3+} acceptor level is empty, thus the nominal oxidation state is Co^{4+} and no charge carrier is present. Upon warming, such impurity level becomes gradually occupied by the electrons originated from the lower Hubbard band due to the thermal energy, shifting the Co oxidation state towards the Co^{3+} side and hole-doping the lower Hubbard band. The density of states of the lower Hubbard band nearby E_F is

$$n(E') = (1/4\pi^2)(2m^*/\hbar^2)^{3/2}\sqrt{E'}, \quad (1)$$

where $E' \equiv |E - E_F|$ and m^* is the lower Hubbard band effective mass⁶⁵. The number of thermally-activated holes per unit volume

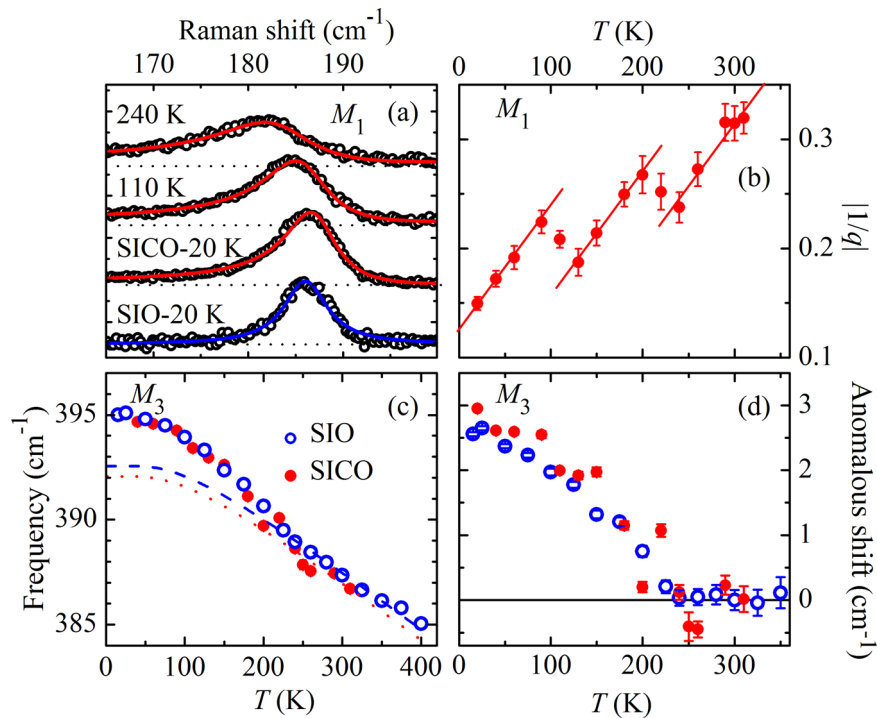


Fig. 5 Temperature-dependent Raman scattering. **a** Raman spectrum of Sr₂Ir_{0.95}Co_{0.05}O₄ (SICO) at selected temperatures and Sr₂IrO₄ (SIO) at 20 K in the vicinity of the M₁ peak (symbols, see also Fig. 2c). The solid lines are fits to an asymmetric Fano lineshape for SICO and a symmetric Lorentzian lineshape for SIO. Data were vertically translated for clarity. The horizontal dotted lines represent the baseline for each spectrum. **b** Modulus of the Fano asymmetry parameter $|1/q|$ of the M₁ peak of SICO. The straight lines with equal angular coefficients are guides to the eye. **c** Frequency of the M₃ mode of SIO (open circles) and SICO (closed circles). The dashed and dotted lines indicate the expected anharmonic behavior for SIO and SICO, respectively⁶¹. **d** Anomalous M₃ phonon shift, defined as the difference between the observed frequencies and the anharmonic contributions shown in (c). The errorbars in (b, d) are standard deviations extracted from the fits, which are smaller than the symbol sizes in (c).

at low temperatures is

$$N(T) = \int_0^{\infty} n(E') e^{-E'/k_B T} dE' = (1/4\pi^2)(2m^*/\hbar^2)^{3/2} \Gamma(3/2)(k_B T)^{3/2}, \quad (2)$$

where $\Gamma(u)$ is the gamma function. These carriers have mean energy $\bar{E}(T) = 3k_B T/2$. We now treat these thermally-activated holes semiclassically with a renormalized mass m_{ren} that is not necessarily equal to m^* . The time between collisions is

$$\tau = D/\bar{v} = D\sqrt{m_{\text{ren}}/2\bar{E}(T)} = D\sqrt{m_{\text{ren}}/3k_B T}, \quad (3)$$

where D is the carrier mean free path. From the Drude relation $\sigma(T) = q^2 N(T)\tau/m_{\text{ren}}$, where q is the electron charge, we obtain

$$\sigma(T) = (\Gamma(3/2)/\sqrt{6\pi^2})[q^2(m^*)^{3/2}D/\hbar^3(m_{\text{ren}})^{1/2}]k_B T. \quad (4)$$

Thus, this simple model is able to reproduce the observed power-law behavior for the electrical conductivity $\sigma(T) = AT^x$ with the correct exponent $x = 1$. Also, the experimental coefficient $A = 0.315\Omega^{-1}\text{m}^{-1}\text{K}^{-1}$ (see Fig. 3b) can be used to obtain further information on

$$m_{\text{ren}} = (\Gamma^2(3/2)/6\pi^4)(q^4 k_B^2/\hbar^6)[(m^*)^3 D^2/A^2]. \quad (5)$$

Using $D \sim 8 \text{ \AA}$ (see above) and considering that $m^* > m_e$, we obtain $m_{\text{ren}} \gtrsim 700 m_e$, where m_e is the free electron mass! Such a huge estimated renormalized mass is indicative of heavy-fermion physics. Indeed, the energy diagram displayed in Fig. 1c, with a localized impurity level near E_F , suggests an analogy with heavy-fermion materials with localized $4f$ levels near E_F . The important difference here is that the “conduction electrons” are actually

thermally-excited QCF. The absence of charge carriers as $T \rightarrow 0$ means there is no Sommerfeld coefficient γ for the specific heat $c_p(T)$ associated with the QCF captured by our model. Rather, the low-temperature $c_p(T)$ from the QCF should actually scale with $d[N(T)\bar{E}(T)]/dT \propto T^{3/2}$, possibly mixing with magnon contributions. These considerations imply that the linear $\sigma(T)$ curve presented here is likely the most direct macroscopic manifestation of the QCF in SICO.

The observation of QCF in SICO, with similar $T_N \sim 240 \text{ K}$ and pseudospin-phonon coupling strength in comparison to SIO, demonstrates that the quantum critical points associated with the charge transport and magnetic transitions are distinct in these iridates. This is reasonable once a non-zero density of charge carriers is presumably necessary to destroy the magnetic ordering at $T = 0 \text{ K}$. The thermally-activated holes possess charge and spin-orbital degrees of freedom, and this system offers an opportunity to access the resulting QCF in the magnetically ordered regime.

Conclusion

In summary, a detailed analysis of our electrical resistivity and Raman scattering data uncovers the presence of QCF in SICO. The inferred quantum phase transition is related to the crossing of the Co³⁺ acceptor level with the top of the lower $J_{\text{eff}} = 1/2$ band at E_F . The linear behavior observed in $\sigma(T)$ is captured by a Drude-like semiclassical model that indicates a large renormalized electron mass for the thermally-activated charge carriers.

Methods

Sample synthesis. The Sr₂IrO₄ (SIO) and Sr₂Ir_{0.95}Co_{0.05}O₄ (SICO) polycrystalline samples were synthesized by a standard solid-state reaction method employing high-purity SrCO₃, IrO₂ and CoO as described in ref. ²⁶. Since the reagents are

mixed in stoichiometric proportions, this method leaves minimum margin for compositional Sr/Ir/Co variations, which is critical for the conclusions of this work. Also, the large absolute resistivity values at low temperatures of SIO, and especially the large low- T /high- T ratio $\rho(50\text{ K})/\rho(300\text{ K}) \sim 10^4$ (see Fig. 3a) compares to the highest reported values in the literature³⁰, unfavoring the possibility of any relevant doping due to off-stoichiometric oxygen content in this sample. This conclusion is likely extensible to SICO, considering that both samples were synthesized by the same procedure.

X-ray diffraction and energy-dispersive X-ray spectroscopy. Laboratory X-ray diffraction data were taken in a Bruker D2 diffractometer equipped with a linear detector, employing Cu $K\alpha$ radiation ($\lambda = 1.542\text{ \AA}$). Rietveld refinements were performed with the GSAS-II suite⁶⁶. The refined Co occupancy at the Ir site is 4.2 (7%) for SICO, close to the 5% nominal value. The other refined crystallographic parameters are given in the Supplementary Table S1. Energy-dispersive X-ray spectroscopy measurements were performed on two different spots of SICO using a scanning electron microscope FEI Nanolab 200 and confirm a homogeneous Co concentration of 5(1)%. Synchrotron X-ray powder diffraction measurements at ambient temperature were also carried out at the XDS beamline of the Brazilian Synchrotron Light Laboratory (LNLS)⁶⁷ with $\lambda = 0.61986\text{ \AA}$ employing the experimental setup described in ref. 27. The structure illustrations in Fig. 1 were produced with the aid of the program VESTA⁶⁸.

Electrical and magnetic measurements. Electrical resistivity and magnetoresistance were measured using a standard four-point technique with a dc bridge in an applied magnetic field up to $H = 90\text{ kOe}$ in a commercial system. The dc -magnetization measurements were performed with a Superconducting Quantum Interference Device magnetometer (SQUID) and a SQUID with a Vibrating Sample Magnetometer (SQUID-VSM).

Raman scattering. Raman scattering experiments were performed in a quasi-backscattering geometry using the 488.0 nm line of Ar⁺ laser with focus spot size $\sim 50\text{ }\mu\text{m}$. The laser power was kept below 20 mW. A Jobin-Yvon T64000 triple-grating spectrometer with 1800 mm^{-1} gratings was employed. A LN₂-cooled multichannel charge-coupled device was used to collect and process the scattered data. The sample was mounted on a cold finger of closed-cycle He cryostat with base temperature 20 K.

Data availability

The authors declare that the main data supporting the findings of this study are available within the article and its Supplementary Information file. Extra data are available from the corresponding author upon reasonable request.

Received: 14 November 2020; Accepted: 1 April 2021;

Published online: 10 May 2021

References

- Okamoto, Y., Nohara, M., Aruga-Katori, H. & Takagi, H. Spin-liquid state in the $S = 1/2$ hyperkagome antiferromagnet $\text{Na}_4\text{Ir}_3\text{O}_8$. *Phys. Rev. Lett.* **99**, 137207 (2007).
- Jackeli, G. & Khaliullin, G. Mott insulators in the strong spin-orbit coupling limit: from Heisenberg to a quantum compass and Kitaev models. *Phys. Rev. Lett.* **102**, 017205 (2009).
- Price, C. C. & Perkins, N. B. Critical properties of the Kitaev-Heisenberg model. *Phys. Rev. Lett.* **109**, 187201 (2012).
- Singh, Y. et al. Relevance of the Heisenberg-Kitaev model for the honeycomb lattice iridates A_2IrO_3 . *Phys. Rev. Lett.* **108**, 127203 (2012).
- Wang, F. & Senthil, T. Twisted Hubbard model for Sr_2IrO_4 : Magnetism and possible high temperature superconductivity. *Phys. Rev. Lett.* **106**, 136402 (2011).
- Watanabe, H., Shirakawa, T. & Yunoki, S. Monte Carlo study of an unconventional superconducting phase in iridium oxide $J_{\text{eff}} = 1/2$ mott insulators induced by carrier doping. *Phys. Rev. Lett.* **110**, 027002 (2013).
- Meng, Z. Y., Kim, Y. B. & Kee, H.-Y. Odd-parity triplet superconducting phase in multiorbital materials with a strong spin-orbit coupling: Application to doped Sr_2IrO_4 . *Phys. Rev. Lett.* **113**, 177003 (2014).
- Kim, Y. K. et al. Fermi arcs in a doped pseudospin-1/2 Heisenberg antiferromagnet. *Science* **345**, 187–190 (2014).
- Yan, Y. J. et al. Electron-doped Sr_2IrO_4 : an analogue of hole-doped cuprate superconductors demonstrated by scanning tunneling microscopy. *Phys. Rev. X* **5**, 041018 (2015).
- Kim, Y. K., Sung, N. H., Denlinger, J. D. & Kim, B. J. Observation of a d -wave gap in electron-doped Sr_2IrO_4 . *Nature Physics* **12**, 37–41 (2016).
- Cao, G. et al. Electrical control of structural and physical properties via strong spin-orbit interactions in Sr_2IrO_4 . *Phys. Rev. Lett.* **120**, 017201 (2018).
- Ye, F., Hoffmann, C., Tian, W., Zhao, H. & Cao, G. Pseudospin-lattice coupling and electric control of the square-lattice iridate Sr_2IrO_4 . *Phys. Rev. B* **102**, 115120 (2020).
- Crawford, M. K. et al. Structural and magnetic studies of Sr_2IrO_4 . *Phys. Rev. B* **49**, 9198–9201 (1994).
- Huang, Q. et al. Neutron powder diffraction study of the crystal structures of Sr_2RuO_4 and Sr_2IrO_4 at room temperature and at 10 K. *Journal of Solid State Chemistry* **112**, 355–361 (1994).
- Moon, S. J. et al. Dimensionality-controlled insulator-metal transition and correlated metallic state in $5d$ transition metal oxides $\text{Sr}_{n+1}\text{Ir}_n\text{O}_{3n+1}$ ($n = 1, 2$, and ∞). *Phys. Rev. Lett.* **101**, 226402 (2008).
- Kim, B. J. et al. Phase-sensitive observation of a spin-orbital Mott state in Sr_2IrO_4 . *Science* **323**, 1329–1332 (2009).
- Arita, R., Kuneš, J., Kozhevnikov, A. V., Eguiluz, A. G. & Imada, M. Ab initio studies on the interplay between spin-orbit interaction and coulomb correlation in Sr_2IrO_4 and Ba_2IrO_4 . *Phys. Rev. Lett.* **108**, 086403 (2012).
- Ye, F. et al. Magnetic and crystal structures of Sr_2IrO_4 : a neutron diffraction study. *Phys. Rev. B* **87**, 140406 (2013).
- Boseggia, S. et al. Locking of iridium magnetic moments to the correlated rotation of oxygen octahedra in Sr_2IrO_4 revealed by X-ray resonant scattering. *Journal of Physics: Condensed Matter* **25**, 422202 (2013).
- Ge, M. et al. Lattice-driven magnetoresistivity and metal-insulator transition in single-layered iridates. *Phys. Rev. B* **84**, 100402 (2011).
- Wang, J. C. et al. Decoupling of the antiferromagnetic and insulating states in Tb-doped Sr_2IrO_4 . *Phys. Rev. B* **92**, 214411 (2015).
- Dobrosavljevic, V., Trivedi, N. & Valles, J. M. *Conductor-Insulator Quantum Phase Transitions*. (Oxford University Press, 2012).
- Sachdev, S. Quantum magnetism and criticality. *Nat. Phys.* **4**, 173–185 (2008).
- Haskel, D. et al. Pressure tuning of the spin-orbit coupled ground state in Sr_2IrO_4 . *Phys. Rev. Lett.* **109**, 027204 (2012).
- Zocco, D. A. et al. Persistent non-metallic behavior in Sr_2IrO_4 and $\text{Sr}_3\text{Ir}_2\text{O}_7$ at high pressures. *J. Phys.* **26**, 255603 (2014).
- Samanta, K., Ardito, F. M., Souza-Neto, N. M. & Granado, E. First-order structural transition and pressure-induced lattice/phonon anomalies in Sr_2IrO_4 . *Phys. Rev. B* **98**, 094101 (2018).
- Samanta, K., Tartaglia, R., Kaneko, U. F., Souza-Neto, N. M. & Granado, E. Anisotropic lattice compression and pressure-induced electronic phase transitions in Sr_2IrO_4 . *Phys. Rev. B* **101**, 075121 (2020).
- Haskel, D. et al. Possible quantum paramagnetism in compressed Sr_2IrO_4 . *Phys. Rev. Lett.* **124**, 067201 (2020).
- Chen, C. et al. Persistent insulating state at megabar pressures in strongly spin-orbit coupled Sr_2IrO_4 . *Phys. Rev. B* **101**, 144102 (2020).
- Klein, Y. & Terasaki, I. Insight on the electronic state of Sr_2IrO_4 revealed by cationic substitutions. *J. Phys.* **20**, 295201 (2008).
- Qi, T. F. et al. Spin-orbit tuned metal-insulator transitions in single-crystal $\text{Sr}_2\text{Ir}_{1-x}\text{Rh}_x\text{O}_4$ ($0 \leq x \leq 1$). *Phys. Rev. B* **86**, 125105 (2012).
- Clancy, J. P. et al. Dilute magnetism and spin-orbital percolation effects in $\text{Sr}_2\text{Ir}_{1-x}\text{Rh}_x\text{O}_4$. *Phys. Rev. B* **89**, 054409 (2014).
- Ye, F. et al. Structure symmetry determination and magnetic evolution in $\text{Sr}_2\text{Ir}_{1-x}\text{Rh}_x\text{O}_4$. *Phys. Rev. B* **92**, 201112 (2015).
- Brouet, V. et al. Transfer of spectral weight across the gap of Sr_2IrO_4 induced by La doping. *Phys. Rev. B* **92**, 081117 (2015).
- Chikara, S. et al. $\text{Sr}_2\text{Ir}_{1-x}\text{Rh}_x\text{O}_4$ ($x < 0.5$): An inhomogeneous $J_{\text{eff}} = \frac{1}{2}$ Hubbard system. *Phys. Rev. B* **92**, 081114 (2015).
- Cao, Y. et al. Hallmarks of the Mott-metal crossover in the hole-doped pseudospin-1/2 Mott insulator Sr_2IrO_4 . *Nat. Commun.* **7**, 11367 (2016).
- Sohn, C. H. et al. X-ray absorption spectroscopy study of the effect of Rh doping in Sr_2IrO_4 . *Sci. Rep.* **6**, 23856 (2016).
- Chikara, S. et al. Charge partitioning and anomalous hole doping in Rh-doped Sr_2IrO_4 . *Phys. Rev. B* **95**, 060407 (2017).
- Louat, A. et al. Formation of an incoherent metallic state in Rh-doped Sr_2IrO_4 . *Phys. Rev. B* **97**, 161109 (2018).
- Xu, B. et al. Optical signature of a crossover from Mott- to Slater-type gap in $\text{Sr}_2\text{Ir}_{1-x}\text{Rh}_x\text{O}_4$. *Phys. Rev. Lett.* **124**, 027402 (2020).
- Zwartsenberg, B. et al. Spin-orbit-controlled metal-insulator transition in Sr_2IrO_4 . *Nat. Phys.* **16**, 290–294 (2020).
- Ou, X. & Wu, H. Coupled charge-spin-orbital state in Fe- or Co-doped Sr_2IrO_4 . *Phys. Rev. B* **89**, 035138 (2014).
- Mikhailova, D. et al. Charge transfer and structural anomaly in stoichiometric layered perovskite $\text{Sr}_2\text{Co}_{0.5}\text{Ir}_{0.5}\text{O}_4$. *Eur. J. Inorg. Chem.* **2017**, 587–595 (2017).

44. Chin, Y.-Y. et al. Relation between the Co-O bond lengths and the spin state of Co in layered cobaltates: a high-pressure study. *Sci. Rep.* **7**, 3656 (2017).
45. Agrestini, S. et al. Probing the $J_{\text{eff}}=0$ ground state and the Van Vleck paramagnetism of the Ir^{5+} ions in layered $\text{Sr}_2\text{Co}_{0.5}\text{Ir}_{0.5}\text{O}_4$. *Phys. Rev. B* **97**, 214436 (2018).
46. Gatimu, A. J., Berthelot, R., Muir, S., Sleight, A. W. & Subramanian, M. Synthesis and characterization of $\text{Sr}_2\text{Ir}_{1-x}\text{M}_x\text{O}_4$ ($M=\text{Ti, Fe, Co}$) solid solutions. *J. Solid State Chem.* **190**, 257–263 (2012).
47. Estevez-Rams, E., Leoni, M., Scardi, P., Aragon-Fernandez, B. & Fuess, H. On the powder diffraction pattern of crystals with stacking faults. *Philosophical Magazine* **83**, 4045–4057 (2003).
48. Sung, N. H. et al. Crystal growth and intrinsic magnetic behaviour of Sr_2IrO_4 . *Philosophical Magazine* **96**, 413–426 (2016).
49. Glamazda, A. et al. Effects of hole doping on magnetic and lattice excitations in $\text{Sr}_2\text{Ir}_{1-x}\text{Ru}_x\text{O}_4$ ($x=0-0.2$). *Phys. Rev. B* **89**, 104406 (2014).
50. Mott, N. *Conduction in Non-Crystalline Materials*. (Oxford: Clarendon Press, 1993).
51. Schlottmann, P. Non-Fermi liquid behavior in heavy fermion systems. vol. 23 of *Handbook of Magnetic Materials*, 85–160 (Elsevier, 2015). <https://www.sciencedirect.com/science/article/pii/B9780444635280000024>.
52. Paschen, S. & Si, Q. Quantum phases driven by strong correlations. *Nat. Rev. Phys.* **3**, 9–26 (2021).
53. Bhatti, I. N., Rawat, R., Banerjee, A. & Pramanik, A. K. Temperature evolution of magnetic and transport behavior in 5d Mott insulator Sr_2IrO_4 : significance of magneto-structural coupling. *J. Phys.* **27**, 016005 (2014).
54. Porras, J. et al. Pseudospin-lattice coupling in the spin-orbit Mott insulator Sr_2IrO_4 . *Phys. Rev. B* **99**, 085125 (2019).
55. Cao, G., Bolivar, J., McCall, S., Crow, J. E. & Guertin, R. P. Weak ferromagnetism, metal-to-nonmetal transition, and negative differential resistivity in single-crystal Sr_2IrO_4 . *Phys. Rev. B* **57**, R11039–R11042 (1998).
56. Fano, U. Effects of configuration interaction on intensities and phase shifts. *Phys. Rev.* **124**, 1866–1878 (1961).
57. Gretarsson, H. et al. Two-magnon Raman scattering and pseudospin-lattice interactions in Sr_2IrO_4 and $\text{Sr}_3\text{Ir}_2\text{O}_7$. *Phys. Rev. Lett.* **116**, 136401 (2016).
58. Cetin, M. F. et al. Crossover from coherent to incoherent scattering in spin-orbit dominated Sr_2IrO_4 . *Phys. Rev. B* **85**, 195148 (2012).
59. Chikara, S. et al. Giant magnetoelectric effect in the $J_{\text{eff}} = \frac{1}{2}$ Mott insulator Sr_2IrO_4 . *Phys. Rev. B* **80**, 140407 (2009).
60. Bhatti, I. N. & Pramanik, A. Insight into the magnetic behavior of Sr_2IrO_4 : a spontaneous magnetization study. *Phys. Lett. A* **383**, 1806–1809 (2019).
61. Balkanski, M., Wallis, R. F. & Haro, E. Anharmonic effects in light scattering due to optical phonons in silicon. *Phys. Rev. B* **28**, 1928–1934 (1983).
62. Baltensperger, W. & Helman, J. S. Influence of magnetic order in insulators on optical phonon frequency. *Helv. Phys. Acta* **41**, 668 (1968).
63. Granado, E. et al. Magnetic ordering effects in the Raman spectra of $\text{La}_{1-x}\text{Mn}_x\text{O}_3$. *Phys. Rev. B* **60**, 11879–11882 (1999).
64. Samanta, K., Rigitano, D., Pagliuso, P. G. & Granado, E. Isospin-phonon coupling and Fano-interference in spin-orbit Mott insulator Sr_2IrO_4 . *Appl. Phys. Lett.* **114**, 152402 (2019).
65. Ashcroft, N. W. & Mermin, N. D. *Solid State Physics* (Harcourt College Publishers, 1976).
66. Toby, B. H. & Von Dreele, R. B. GSAS-II: the genesis of a modern open-source all purpose crystallography software package. *J. Appl. Crystallogr.* **46**, 544–549 (2013).
67. Lima, F. A. et al. XDS: a flexible beamline for X-ray diffraction and spectroscopy at the Brazilian synchrotron. *J. Synchrotron Radiat.* **23**, 1538–1549 (2016).
68. Momma, K. & Izumi, F. VESTA3 for three-dimensional visualization of crystal, volumetric and morphology data. *J. Appl. Crystallogr.* **44**, 1272–1276 (2011).

Acknowledgements

We would like to acknowledge M. A. Avila for providing assistance in the SQUID-VSM measurements. This work was supported by Fapesp Grants 2016/00756-6, 2017/10581-1, 2018/20142-8, 2018/11364-7, and 2018/18653-4, as well as CNPq Grants 308607/2018-0, 304496/2017-0, and 409504/2018-1, Brazil. LNLS is acknowledged for the concession of beamtime. The authors also acknowledge the Center for Semiconducting Compounds and Nanotechnologies (CCS) at UNICAMP for providing the equipment and technical support for the energy-dispersive X-ray spectroscopy measurements.

Author contributions

K.S., J.C.S., P.G.P., and E.G. conceived the experiments. Experimental data were taken by K.S., J.C.S., D.R., and A.I.M. under supervision of P.G.P. and E.G. Data analysis was performed by K.S., J.C.S., A.I.M., and E.G. The model was developed by E.G. The paper was written by K.S. and E.G. with input from all authors.

Competing interests

The authors declare no competing interests.

Additional information

Supplementary information The online version contains supplementary material available at <https://doi.org/10.1038/s42005-021-00591-7>.

Correspondence and requests for materials should be addressed to E.G.

Reprints and permission information is available at <http://www.nature.com/reprints>

Publisher's note Springer Nature remains neutral with regard to jurisdictional claims in published maps and institutional affiliations.



Open Access This article is licensed under a Creative Commons Attribution 4.0 International License, which permits use, sharing, adaptation, distribution and reproduction in any medium or format, as long as you give appropriate credit to the original author(s) and the source, provide a link to the Creative Commons license, and indicate if changes were made. The images or other third party material in this article are included in the article's Creative Commons license, unless indicated otherwise in a credit line to the material. If material is not included in the article's Creative Commons license and your intended use is not permitted by statutory regulation or exceeds the permitted use, you will need to obtain permission directly from the copyright holder. To view a copy of this license, visit <http://creativecommons.org/licenses/by/4.0/>.

© The Author(s) 2021